Journal of Catalysis 287 (2012) 149–160

Contents lists available at SciVerse ScienceDirect

Journal of Catalysis

journal homepage: www.elsevier.com/locate/jcat

Controlled preparation and high catalytic performance of three-dimensionally ordered macroporous $LaMnO_3$ with nanovoid skeletons for the combustion of toluene

Yuxi Liu [a], Hongxing Dai [a,*], Yucheng Du [b], Jiguang Deng [a], Lei Zhang [a], Zhenxuan Zhao [a], Chak Tong Au [c]

[a] Laboratory of Catalysis Chemistry and Nanoscience, Department of Chemistry and Chemical Engineering, College of Environmental and Energy Engineering, Beijing University of Technology, Beijing 100124, China
[b] Key Lab of Advanced Functional Materials, Ministry of Education, College of Materials Science and Engineering, Beijing University of Technology, Beijing 100124, China
[c] Department of Chemistry, Hong Kong Baptist University, Kowloon Tong, Kowloon, Hong Kong, China

ARTICLE INFO

Article history:
Received 1 October 2011
Revised 16 December 2011
Accepted 18 December 2011
Available online 25 January 2012

Keywords:
Surfactant-assisted poly(methyl methacrylate)-templating strategy
Three-dimensionally ordered macroporous perovskite-type oxides
Lanthanum manganate
Nanovoid skeletons
Toluene combustion

ABSTRACT

Three-dimensionally ordered macroporous (3DOM) single-phase rhombohedral perovskite-type oxide $LaMnO_3$ materials with nanovoid skeletons were prepared using the poly(methyl methacrylate)-templating methods with the assistance of surfactant (poly(ethylene glycol) (PEG) or triblock copolymer (Pluronic P123)). The nature of surfactant influenced the pore structure of the $LaMnO_3$ sample. The use of PEG400 alone led to a 3DOM-structured $LaMnO_3$ without nanovoid skeletons; with the addition of PEG400 and P123, however, one could prepare $LaMnO_3$ samples with high-quality 3DOM structures, nanovoid skeletons, and high surface areas (37–39 m^2/g). Under the conditions of toluene concentration = 1000 ppm, toluene/O_2 molar ratio = 1:400, and space velocity = 20,000 mL/(g h), the porous $LaMnO_3$ samples were superior to the bulk counterpart in catalytic performance, with the nanovoid-containing 3DOM-structured $LaMnO_3$ catalyst performing the best (the temperatures for toluene conversions of 50% and 90% were 222–232 and 243–253 °C, respectively). The apparent activation energies (57–62 kJ/mol) over the 3DOM-structured $LaMnO_3$ catalysts were much lower than that (97 kJ/mol) over the bulk $LaMnO_3$ catalyst. We believe that the excellent performance of the 3D macroporous $LaMnO_3$ materials in catalyzing the combustion of toluene might be due to factors such as large surface area, high oxygen adspecies concentration, good low-temperature reducibility, and unique nanovoid-containing 3DOM structure of the materials.

1. Introduction

Most of the volatile organic compounds (VOCs) are air pollutants harmful to human health. They can be removed by means of catalytic combustion. In the past years, supported noble metals [1], single or mixed transition metal oxides [2], and perovskite-type oxides (ABO_3) [3] have been utilized for the combustion of VOCs. Although supported precious metals (e.g., Pt and Pd) can catalyze the oxidation of various VOCs at lower temperatures [1], the high cost and limited availability of noble metals restrict their wide applications. ABO_3 are known to be catalytically active for the complete oxidation of hydrocarbons and oxygenates [3]. Among the ABO_3 catalysts, cobaltate and manganate perovskites show good activities in catalyzing the combustion of VOCs. Najjar and Batis [4] observed an ethanol conversion of 90% over $LaMnO_3$ at 202 °C and 60,000 mL/(g h). Porta and coworkers [5] claimed that a benzene conversion of 90% was achieved over $LaMnO_3$ at ca. 335 °C and 14,000 h^{-1}. The oxidation of toluene is usually adopted as a model reaction for the evaluation of catalyst performance due to its hard elimination. Irusta et al. [6] examined the catalytic activity of $LaMnO_3$ for the combustion of toluene and found that a toluene conversion of 90% could be achieved at ca. 295 °C and 178 h^{-1}. Over a nanosized $LaMnO_{3.12}$ catalyst under the reaction conditions of 295 °C and 20,000 h^{-1}, we observed a toluene conversion of 80% [7].

It is well known that catalytic activities of ABO_3 are associated with factors such as oxygen nonstoichiometry, reducibility, surface area, and pore structure [8–10]. The preservation of high surface area is critical because the reaction rate has often been observed to be directly proportional to the surface area of a bulk perovskite catalyst, especially in the case of combustion of hydrocarbons [11]. The ABO_3 materials prepared via the citric acid-complexing [12], co-precipitation [13], and solid-state reaction [14] routes are usually nonporous and relatively low in surface area (<10 m^2/g), making the accessibility of reactant molecules to the active sites

* Corresponding author. Fax: +86 10 6739 1983.
E-mail address: hxdai@bjut.edu.cn (H. Dai).

0021-9517/$ - see front matter © 2011 Elsevier Inc. All rights reserved.
doi:10.1016/j.jcat.2011.12.015

unfavorable. It is hence highly desirable to develop a strategy that is effective for the preparation of ABO_3 with porous structures and high surface areas in a controlled manner.

Up to now, there have been several reports on the preparation of high-surface-area porous ABO_3. For example, Wang et al. [9] synthesized ordered mesoporous $LaCoO_3$ with a surface area of ca. 97 m^2/g via an ordered mesoporous silica-nanocasting route. Through the use of block copolymer Pluronic PE 10300, Hou et al. [15] prepared nanoporous $BaTiO_3$ with a surface area of 70 m^2/g. By adopting the evaporation-induced self-assembling (EISA) method, Fan et al. [16] fabricated mesoporous $SrTiO_3$ and $BaTiO_3$ having surface areas of up to 206 and 167 m^2/g, respectively. In recent years, three-dimensional-ordered macroporous (3DOM) materials with unique 3D pore structures and large surface areas have attracted much attention due to their potential catalytic applications. Using metal nitrates or acetates as precursors and well-arrayed polymethyl methacrylate (PMMA) or polystyrene (PS) microspheres as hard templates, Sadakane et al. [17] and Kim et al. [18] prepared 3DOM-structured $La_{1-x}Sr_xFeO_3$ (surface area = 24–49 m^2/g) and $La_{0.7}Ca_{0.3-x}Sr_xMnO_3$ (ca. 24 m^2/g), respectively. Zhao and coworkers [19,20] synthesized a series of 3DOM $Au/LaFeO_3$ (surface area = 31–32 m^2/g) and $LaCo_xFe_{1-x}O_3$ catalysts, which exhibited super catalytic performance (the temperature required for 50% soot conversion was 359 °C over 6.3 wt.% $Au/LaFeO_3$ and 397 °C over $LaCo_{0.5}Fe_{0.5}O_3$).

All of the mentioned 3DOM-structured perovskites, however, possessed no mesoporous or nanovoids in the walls, leading to relatively low surface areas. Although silica [21] and carbon [22] with a bimodal distribution of meso- and macropores could be fabricated, the controlled preparation and catalytic application of 3DOM-structured $LaMnO_3$ materials with mesoporous or nanovoid-like crystalline walls for the combustion of toluene have not been reported in the literature.

In the past years, our group investigated the fabrication, characterization, and physicochemical properties of high-surface-area magnesia [23], calcium oxide [24], alumina [25], and iron oxide [26] by using the surfactant-templating or surfactant-assisted PMMA-templating strategy. We observed that the introduction of a surfactant during the preparation process was beneficial for the generation of mesoporous or nanovoid-like walls and thus beneficial for the improvement of physicochemical property [24,25]. Recently, we extended our attention to the catalysis of 3DOM-structured ABO_3 and perovskite-like oxides (A_2BO_4) of high surface area for the oxidation of VOCs. In this paper, we report the preparation and catalytic properties of 3DOM-structured $LaMnO_3$ with nanovoid skeletons for the combustion of toluene.

2. Experimental

2.1. Catalyst preparation

The well-arrayed hard template PMMA microspheres with an average diameter of ca. 300 nm were synthesized according to the procedures described elsewhere [25]. The 3D macroporous $LaMnO_3$ samples were prepared using the surfactant-assisted PMMA-templating strategy. In a typical process, 30 mmol of $La(NO_3)_3{\cdot}6H_2O$ and 30 mmol of $Mn(NO_3)_2$ (50 wt.% aqueous solution) were dissolved in a solution of 3 mL poly(ethylene glycol) (PEG, molecular weight = 400 g/mol) and 3 mL methanol under stirring at room temperature (RT) for 4 h to obtain a transparent solution. Then, 7 mL of a methanol solution containing 1.00, 2.00, or 4.00 g of P123 with an average molecular weight of 5800 g/mol was added to the as-obtained transparent solution that was stirred for 1 h to get a uniform precursor solution. A certain amount of methanol was added to achieve a total metal concentration of 2 mol/L. Then, ca. 2.0 g of the PMMA hard template was soaked in the obtained mixed solution for 4 h. After being filtered out, the obtained wet PMMA template was dried in air at RT for 48 h and then transferred to a ceramic boat that was placed in a tubular furnace. The thermal treatment process was divided into two steps: (i) the dried solid was calcined in a N_2 flow of 50 mL/min at a ramp of 1 °C/min from RT to 300 °C and kept at this temperature for 3 h and then cooled to 50 °C in the same atmosphere and (ii) after being purged in an air flow of 50 mL/min, the solid was heated from RT to 300 °C in the same atmosphere at a ramp of 1 °C/min and held at 300 °C for 2 h and then was heated to 750 °C (at the same ramp) and calcined at 750 °C for 4 h. The as-obtained 3DOM-structured sample was denoted as $LaMnO_3$–PP-1, $LaMnO_3$–PP-2, and $LaMnO_3$–PP-3 (corresponding to the use of PEG400 and P123 with PEG400/P123 molar ratio = 48.7, 24.4, and 12.2), in which "PP" denotes the use of "PEG" and "P123."

The 3DOM-structured $LaMnO_3$ samples without nanovoid-like walls were prepared using the PEG-assisted PMMA-templating or surfactant-free PMMA-templating strategy. In a typical synthesis, no surfactant P123 was added, but other parameters and calcination procedures were the same as those adopted for the preparation of $LaMnO_3$–PP-1–3, the thus-obtained 3DOM sample was denoted as $LaMnO_3$–PEG. By using the same method in the absence of surfactant P123 and PEG, we also prepared the 3DOM-structured $LaMnO_3$ sample (denoted as $LaMnO_3$–MeOH). For comparison purposes, the bulk $LaMnO_3$ sample was prepared via the citric acid-complexing route [12] and after calcination in air at 850 °C for 4 h. For the sake of better presentation, the main preparation conditions of these materials are summarized in Table 1.

All of the chemicals (A.R. in purity) were purchased from Beijing Chemical Company and used without further purification.

2.2. Catalyst characterization

X-ray diffraction (XRD) patterns of the samples were recorded on a Bruker D8 Advance diffractometer with Cu Kα radiation and nickel filter (λ = 0.15406 nm), and the operating voltage and current were 40 kV and 35 mA, respectively. The crystal phases of the samples were identified by referring to the JCPDS Database. Thermogravimetric analysis (TGA) and differential scanning calorimetric (DSC) analysis of the uncalcined samples were conducted (from RT to 900 °C) in an air flow of 50 mL/min at a heating rate of 10 °C/min over a SDT Q600 (TA) apparatus. BET (Brunauer–Emmett–Teller) surface areas of the samples were measured via N_2 adsorption at −196 °C on a Micromeritics ASAP 2020 analyzer with the samples outgassed at 300 °C for 2.5 h under vacuum before measurement. Fourier transform infrared (FT-IR) spectra of the samples (1 wt.% sample + 99 wt.% KBr) were obtained in the region of 400–4000 cm^{-1} with a resolution of 0.4 cm^{-1} on a Bruker Vertex 70 spectrometer. The scanning electron microscopic (SEM) images of the samples were recorded on a Gemini Zeiss Supra 55 apparatus (operating at 10 kV). Transmission electron microscopic (TEM) images of the samples were obtained using the JEOL-2010 equipment (operating at 200 kV). X-ray photoelectron spectroscopy (XPS, VG CLAM 4 MCD analyzer) was used to determine the La 3d, Mn 2p, O 1s, and C 1s binding energies (BEs) of surface species using Mg Kα ($h\nu$ = 1253.6 eV) as the excitation source. The instrumental resolution was 0.5 eV. In order to minimize the amounts of OH^- and carbonate species on the surfaces, the samples were calcined in O_2 (flow rate = 20 mL/min) at 600 °C for 1 h and then cooled in the same atmosphere to RT before XPS measurements. After such a pretreatment, the samples were mounted and transferred to the spectrometer in a transparent Glove Bag (Instruments for Research and Industry, USA) filled with helium. The samples were then outgassed in the preparation chamber (10^{-5} Torr) for 0.5 h and introduced into the analysis chamber (3×10^{-9} Torr)

Table 1
Preparation parameters, particle sizes, BET surface areas, average pore sizes, and pore volumes of the as-obtained $LaMnO_3$ samples.

Catalyst code	Hard template/ surfactant	(La + Mn)/ P123 molar ratio (mol/mol)	PEG400/ P123 molar ratio (mol/mol)	Calcination condition	D^a (nm)	BET surface area (m^2/g)			Pore volume (cm^3/g)	Average pore size (nm)	
						Macropore (>50 nm)	Mesopore (⩽50 nm)	Total		Macropore [b] (>50 nm)	Mesopore (⩽50 nm)
$LaMnO_3$–bulk	–/–	–	–	850 °C 4 h (in air)	118	–	–	7.3	–	–	–
$LaMnO_3$–MeOH	PMMA/–	–	–	300 °C 3 h (in N_2) → 300 °C 2 h (in air) → 750 °C 4 h (in air)	31	1.6	19.8	21.4	0.062	135	7.5
$LaMnO_3$–PEG	PMMA/PEG400	–	–	300 °C 3 h (in N_2) → 300 °C 2 h (in air) → 750 °C 4 h (in air)	37	6.4	25.5	31.9	0.093	140	13.9
$LaMnO_3$–PP-1	PMMA/ (P123 + PEG400)	348/1	48.7/1	300 °C 3 h (in N_2) → 300 °C 2 h (in air) → 750 °C 4 h (in air)	35	4.6	33.1	37.7	0.110	90	14.2
$LaMnO_3$–PP-2	PMMA/ (P123 + PEG400)	174/1	24.4/1	300 °C 3 h (in N_2) → 300 °C 2 h (in air) → 750 °C 4 h (in air)	33	4.7	34.7	39.4	0.113	85	20.0
$LaMnO_3$–PP-3	PMMA/ (P123 + PEG400)	87/1	12.2/1	300 °C 3 h (in N_2) → 300 °C 2 h (in air) → 750 °C 4 h (in air)	27	4.3	32.9	37.2	0.096	80	20.6
$LaMnO_3$–PP-2_850	PMMA/ (P123 + PEG400)	174/1	24.4/1	300 °C 3 h (in N_2) → 300 °C 2 h (in air) → 850 °C 4 h (in air)	47	3.4	23.9	27.3	0.064	85	8.1
$LaMnO_3$–PP-2_950	PMMA/ (P123 + PEG400)	174/1	24.4/1	300 °C 3 h (in N_2) → 300 °C 2 h (in air) → 950 °C 4 h (in air)	72	2.8	16.2	19.0	0.031	65	6.8

[a] Data determined based on XRD results according to the Scherrer's equation.
[b] Estimated based on TEM images.

for spectrum recording. The C 1s signal at 284.6 eV was taken as a reference for BE calibration.

Hydrogen temperature-programmed reduction (H_2-TPR) experiments were carried out on a chemical adsorption analyzer (Autochem II 2920, Micromeritics). Before TPR measurement, ca. 0.02 g of catalyst (40–60 mesh) was first treated in an oxygen flow of 30 mL/min at 500 °C for 1 h in a quartz fixed-bed U-shaped microreactor (i.d. = 4 mm). After being cooled at the same atmosphere to RT, the pretreated sample was exposed to a flow (50 mL/min) of 5% H_2–95% Ar (v/v) mixture and heated from RT to 900 °C at a ramp of 10 °C/min. The variation in H_2 concentration of the effluent was monitored online by the chemical adsorption analyzer. The reduction band was calibrated against that of the complete reduction of a known standard of powdered CuO (Aldrich, 99.995%).

2.3. Catalytic evaluation

A continuous flow fixed-bed quartz microreactor (i.d. = 4 mm) was used to determine the catalytic activities of the samples at atmospheric pressure for the complete oxidation of toluene. To minimize the effect of hot spots, quartz sands (40–60 mesh) with a mass equal to that (0.1–0.2 g) of the catalyst sample were used to dilute the catalyst. The total flow rate of the reactant mixture (1000 ppm toluene + O_2 + N_2 (balance)) was 33.3 mL/min, giving a toluene/O_2 molar ratio of 1:400 and a space velocity (SV) of 20,000 mL/(g h). The 1000-ppm toluene was generated by passing a N_2 flow through a bottle containing pure toluene (A.R. grade) chilled in an ice-water isothermal bath. For the changes in SV and toluene/O_2 molar ratio, we altered the amount of catalyst and mass flow of O_2, respectively. Reactants and products were analyzed online by a gas chromatograph (GC-2010, Shimadzu) equipped with a flame ionization detector (FID) and a thermal conductivity detector (TCD), using a 1/8 in Chromosorb 101 column (3 m in length) for VOCs and a 1/8 in Carboxen 1000 column (3 m in length) for permanent gas separation. By using a mass spectrometer (HPR20, Hiden), we only detected toluene, carbon dioxide, and water in the outlet gas mixture from the microreactor. Based on the peak areas of toluene and carbon dioxide detected by GC-2010, the balance of carbon throughout the investigation was estimated to be 99.5%. The relative errors for the gas concentration measurements were less than ±1.5%.

3. Results and discussion

3.1. Crystal phase structure

Fig. 1 shows the XRD patterns of as-prepared catalysts. By referring to the XRD pattern of standard $LaMnO_3$ sample (JCPDS PDF# 82-1152), one can deduce that all of the as-prepared catalysts were single-phase and of rhombohedral crystal structure. Due to the detection limitation of XRD measurements, we cannot preclude the possible presence of trace amounts of other solid phases (e.g., manganese oxide and/or lanthanum oxide) in the as-prepared samples. The Bragg diffraction peaks in the 2θ range of 10–80° could be well indexed, as indicated in Fig. 1h and Fig. S1 (Supplementary data). It is observed that there was no significant difference in peak intensity across the $LaMnO_3$–MeOH, $LaMnO_3$–PEG, and $LaMnO_3$–PP-1–3 samples, indicating similarity in $LaMnO_3$ crystallinity. With increase of calcination temperature from 750 to 850 or 950 °C (Fig. 1g and h), however, the $LaMnO_3$–PP-2 catalyst showed improvement in crystallinity, reaching that of bulk $LaMnO_3$ that was calcined at 850 °C. The results of TGA/DSC and FT-IR investigations (Figs. S2 and S3 of the Supplementary data, respectively) confirm that the organic species retained in the uncalcined samples were completely removed after the uncalcined samples were thermally treated first in a N_2 flow and then in an air flow at or above 750 °C. According to the XRD line-width data and Scherrer's equation, one can estimate the average particle sizes of the catalysts. It is found that the particle size increased significantly with the rise in calcination temperature (Table 1). For example, the crystallite diameter of 750 °C-calcined $LaMnO_3$–PP-2 was ca. 33 nm, whereas those of the $LaMnO_3$–PP-2_850 and $LaMnO_3$–PP-2_950 samples were ca. 47 and 72 nm, respectively. The results demonstrated that the perovskite structure and crystallinity were predominantly determined by the temperature adopted for thermal treatment.

3.2. Morphology, pore structure, and surface area

Shown in Figs. 2 and 3 are the representative SEM and TEM images as well as the SAED patterns of the as-prepared $LaMnO_3$ samples. It is clear that all of the samples obtained after calcination at 750 °C exhibited a 3DOM architecture. The $LaMnO_3$–MeOH sam-

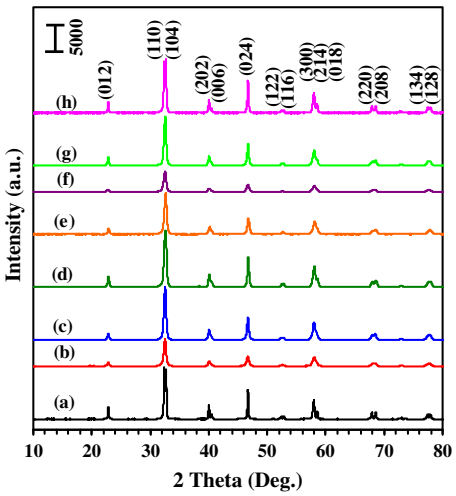

Fig. 1. XRD patterns of (a) $LaMnO_3$–bulk, (b) $LaMnO_3$–MeOH, (c) $LaMnO_3$–PEG, (d) $LaMnO_3$–PP-1, (e) $LaMnO_3$–PP-2, (f) $LaMnO_3$–PP-3, (g) $LaMnO_3$–PP-2_850, and (h) $LaMnO_3$–PP-2_950.

ple derived in the absence of PEG400 and P123 displayed a relatively poor 3DOM structure with a pore-size range of 130–155 nm (Fig. 2a and b). With the addition of PEG400, a high-quality 3DOM-architectured $LaMnO_3$–PEG sample with a pore size of ca. 140 nm (Fig. 2c and d) and a wall thickness of ca. 35 nm (Fig. 3e) was generated. Highly ordered macroporous structures could be obtained via the long-range replication of the 3D close-packed PMMA template [25]. It is known that the polymer templates, which can support the conversion of the metal precursor(s) to a solid-state framework at lower temperatures, play a key role in the successful fabrication of 3DOM metal oxides. In the case of Mn and Co nitrates as metal precursors, the decomposition temperatures of the metal nitrates were comparable to the glass transition temperature of PMMA. Solidification by nitrate decomposition and melting of the PMMA would occur at the same time, and some of the metal salts were squeezed out from the voids in the template and thus causing low fraction of 3DOM structure. Therefore, it would be hard to obtain high-quality 3DOM-structured $LaMnO_3$ materials if only methanol was used as solvent. During the calcination of the PMMA- and PEG400-containing metal nitrates, however, the interaction of the PEG400 and metal nitrates would produce solid metal–PEG complexes [17,27] before the melting of the PMMA template and hence generating the desired 3DOM complex metal oxide intermediates.

Ueda and coworkers prepared 3DOM $LaFeO_3$ with nanovoids on the macropore walls in the presence of methanol and ethylene glycol [27], in which ethylene glycol had an important role to play in the formation of nanovoids on the skeletons of 3DOM $LaFeO_3$. But

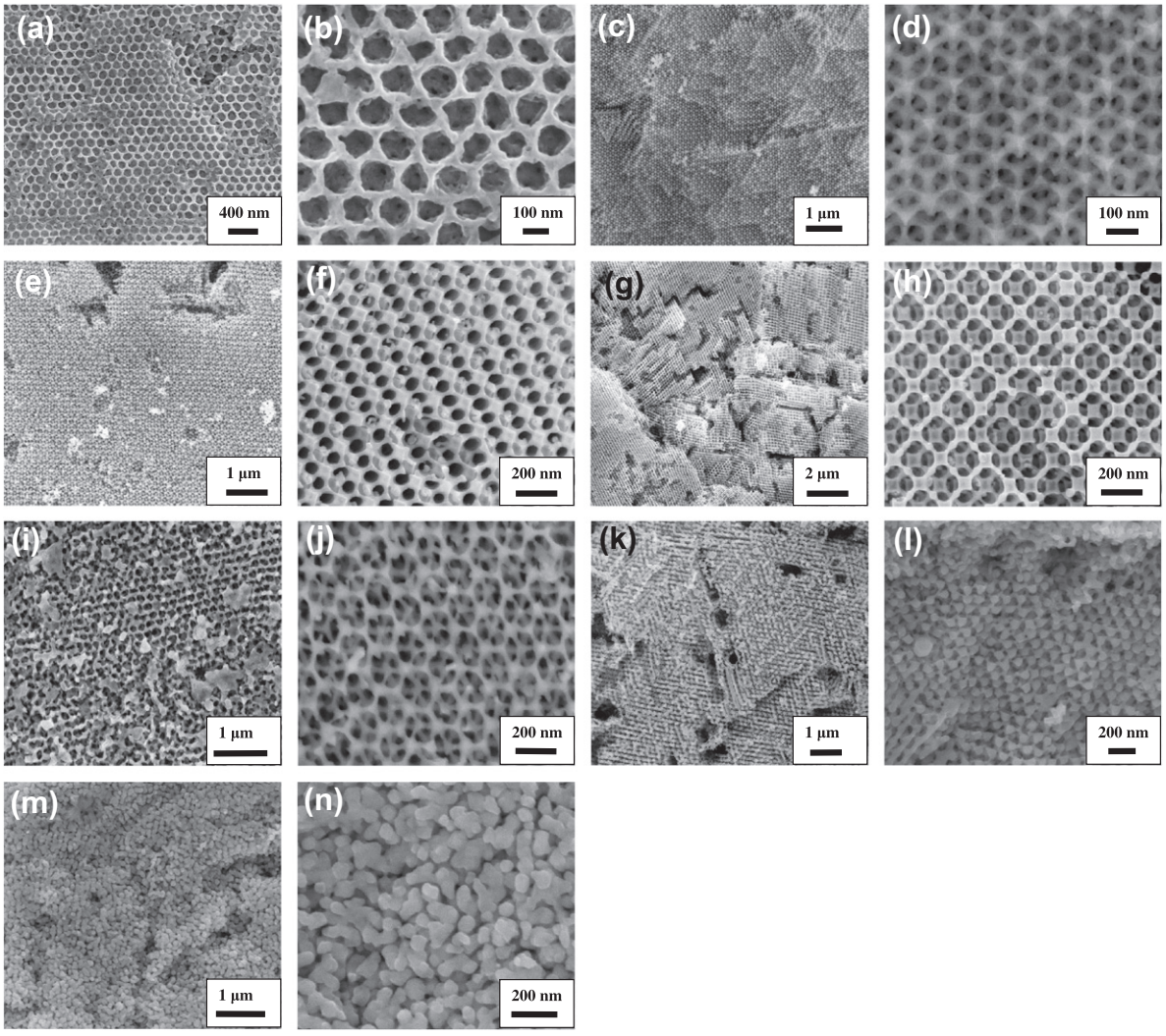

Fig. 2. HRSEM images of (a and b) $LaMnO_3$–MeOH, (c and d) $LaMnO_3$–PEG, (e and f) $LaMnO_3$–PP-1, (g and h) $LaMnO_3$–PP-2, (i and j) $LaMnO_3$–PP-3, (k and l) $LaMnO_3$–PP-2_850, and (m and n) $LaMnO_3$–PP-2_950.

in the presence of methanol and PEG400, we did not observe the existence of nanovoids on the walls of the $LaMnO_3$–PEG sample. With the introduction of P123, however, there was the formation of a number of nanovoids on the walls of the high-quality 3DOM-structured $LaMnO_3$–PP samples, the wall thickness and nanovoid diameters were in the ranges of 19–35 and 3–16 nm, respectively (Fig. 3g, h, j, k, m, and n). A rise in P123 concentration in terms of (La + Mn)/P123 molar ratio from 348 to 174 led to the

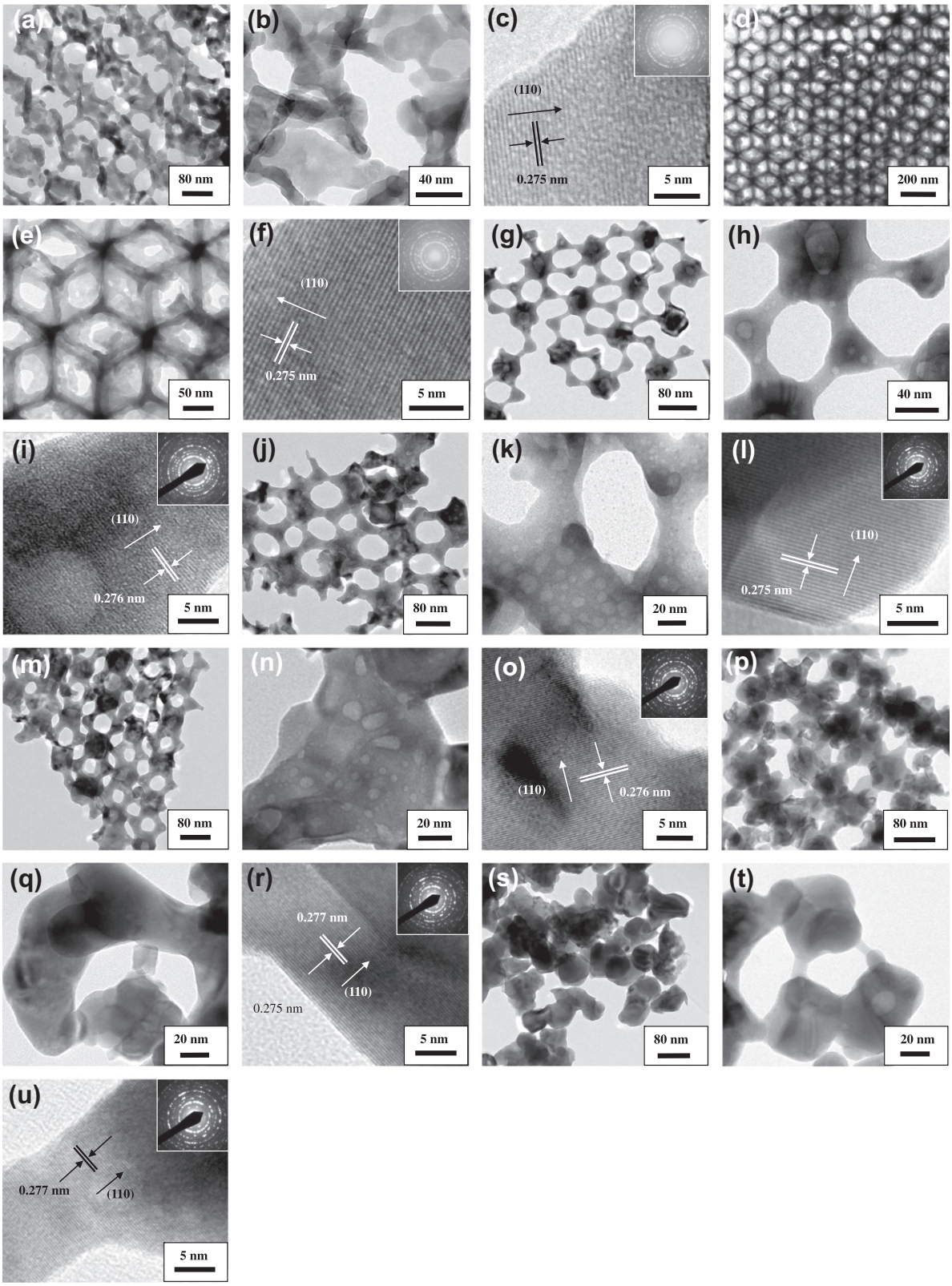

Fig. 3. HRTEM images and SAED patterns (insets) of (a–c) $LaMnO_3$–MeOH, (d–f) $LaMnO_3$–PEG, (g–i) $LaMnO_3$–PP-1, (j–l) $LaMnO_3$–PP-2, (m–o) $LaMnO_3$–PP-3, (p–r) $LaMnO_3$–PP-2_850, and (s–u) $LaMnO_3$–PP-2_950.

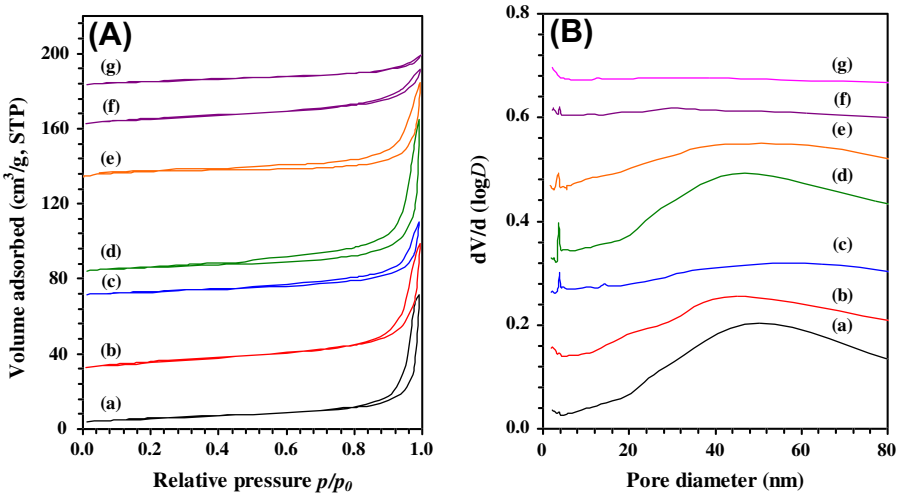

Fig. 4. (A) Nitrogen adsorption–desorption isotherms and (B) pore-size distributions of (a) $LaMnO_3$–MeOH, (b) $LaMnO_3$–PEG, (c) $LaMnO_3$–PP-1, (d) $LaMnO_3$–PP-2, (e) $LaMnO_3$–PP-3, (f) $LaMnO_3$–PP-2_850, and (g) $LaMnO_3$–PP-2_950.

generation of larger amounts of nanovoids on the macropore skeletons of the $LaMnO_3$–PP-2 sample (Fig. 3j and k). A further rise of (La + Mn)/P123 molar ratio from 174 to 87 would result in 3DOM structure worse than that of $LaMnO_3$–PP-2 (Fig. 2i and j). The result reveals that the amount of surfactant P123 had a significant effect on the quality of 3DOM and nanovoid structure on the macropore skeletons. An excessive amount of P123 was unfavorable for the generation of high-quality 3DOM-architectured $LaMnO_3$ materials. Such a result was in agreement with that reported in our previous work [26]. It is worth mentioning that the employment of the calcination procedure (first in N_2 at 300 °C and then in air at 300 and 750 °C) was essential for the formation of the 3DOM structure. The glassy temperature, decomposition temperature, and oxidation temperature of PMMA in air was ca. 130, 290, and 370 °C [25,28], respectively. The PMMA-containing metal precursor was first calcined in N_2 at 300 °C, possibly leading to the partial carbonization of PMMA, the as-resulted amorphous carbon could act as a hard template to prevent macro- and mesoporous structure from collapsing before the polymer template was completely oxidized at a higher temperature [29], thus beneficial for the preservation of 3DOM-structured $LaMnO_3$.

It is well known that the rise in calcination temperature increases the size of solid-state crystallites. If the crystallite size was big enough, the 3DOM structure would collapse [30]. The 3DOM $LaMnO_3$ samples prepared after calcination at 750 °C were smaller in crystallite size (27–37 nm) as compared to the $LaMnO_3$–PP-2_850 sample (47 nm) calcined at 850 °C and the $LaMnO_3$–PP-2_950 sample (72 nm) calcined at 950 °C. Therefore, it is understandable that there was significant destruction of 3DOM structures (Figs. 2k–n, 3p, q, s, and t) and even disappearance of nanovoids on the macropore skeletons of the $LaMnO_3$ samples when calcination temperature was equal to or above 850 °C.

From the high-resolution TEM images of the as-prepared $LaMnO_3$ samples (Fig. 3c, f, i, l, o, r, and u), the lattice spacings (d value) of the (1 1 0) crystal plane were measured to be in the range of 0.275–0.277 nm, not far away from that (0.276 nm) of standard $LaMnO_3$ sample (JCPDS PDF# 82-1152). The observation of multiple bright electron diffraction rings in the SAED patterns (insets of Fig. 3c, f, i, l, o, r, and u) of these $LaMnO_3$ samples suggests the formation of polycrystalline perovskite-phased $LaMnO_3$.

Fig. 4 shows the N_2 adsorption–desorption isotherms and pore-size distributions of the $LaMnO_3$ samples prepared under different conditions, and their BET surface areas and pore properties are summarized in Table 1. It can be seen from Fig. 4A that the N_2 adsorption–desorption isotherm of each sample (except that of the $LaMnO_3$–PP-2_950 sample) was characteristic of a combination of macropore and mesopore structures; the hysteresis loops at the low and high relative pressure ranges vary from sample to sample, reflecting discrepancy in pore-size distribution (Fig. 4B). For the $LaMnO_3$–PP-1, $LaMnO_3$–PP-2, $LaMnO_3$–PP-3, and $LaMnO_3$–PP-2_850 samples, there was a weak but sharp peak at pore diameter = 3.4–4.0 nm (Fig. 4B(c–f) and Fig. S4 of the Supplementary data). On the other hand, a wide pore-size distribution (from 10 to 80 nm) was recorded for the $LaMnO_3$–PEG, $LaMnO_3$–PP-1, $LaMnO_3$–PP-2, and $LaMnO_3$–PP-3 samples. For all of the samples, there might also be the presence of a small amount of micropores in view of the decrease of $dV/d(\log(D))$ with the increase of pore size in the range of 2–4 nm (Fig. S4 of Supplementary data). As can be seen in Table 1, the bulk $LaMnO_3$ sample possesses low surface area (7.3 m^2/g), whereas the porous $LaMnO_3$ samples exhibits much higher surface areas (19–39 m^2/g). With the addition of PEG and/or P123, there is significant increase of surface area (31–39 m^2/g) across the obtained 3DOM-structured $LaMnO_3$ samples, but with the rise of calcination temperature from 750 to 850 or 950 °C, there is decline of surface area due to the partial destruction of 3DOM structure and nanovoids on the macropore skeletons. It should be noted that the use of PEG or P123 caused a change in average pore size of the macropores and nanovoids of the $LaMnO_3$ samples (Table 1).

3.3. Surface composition, Mn oxidation state, and oxygen species

The XPS technique is a powerful tool to investigate the surface element compositions, metal oxidation states, and adsorbed species of solid materials. Table 2 summarizes the surface element compositions of the $LaMnO_3$ samples. It can be observed that the surface La/Mn atomic ratios of the $LaMnO_3$–MeOH and $LaMnO_3$–PEG samples were higher than the nominal (stoichiometric) La/Mn atomic ratio (1.00), indicating La enrichment on the surface of the two samples. The surface La/Mn atomic ratio of the $LaMnO_3$–PP-1 sample was rather close to 1, indicative of the formation of uniform $LaMnO_3$ phase. For the other samples, however, the surface La/Mn atomic ratios were lower than 1.00, suggesting that there was Mn enrichment on the surface of these samples. Similar phenomena were observed by other researchers [13]. The surface

Table 2
Surface element compositions, H_2 consumption, and catalytic activities of as-prepared $LaMnO_3$ samples under the conditions of toluene concentration = 1000 ppm, toluene/oxygen molar ratio = 1:400, and SV = 20,000 mL/(g h).

Catalyst	La/Mn atomic ratio[a]	Mn/(La + Mn + O) atomic ratio[a]	O_{ads}/O_{latt}^{2-} molar ratio	Mn^{4+}/Mn^{3+} molar ratio	H_2 consumption[b] (mmol/g)		Toluene oxidation activity (°C)		
					<500 °C	⩾500 °C	$T_{10\%}$	$T_{50\%}$	$T_{90\%}$
$LaMnO_3$–bulk	1.01 (1.00)	0.19 (0.20)	0.90	1.20	0.97	2.17	220	267	298
$LaMnO_3$–MeOH	1.10 (1.00)	0.17 (0.20)	0.89	1.18	1.45	1.79	201	252	275
$LaMnO_3$–PEG	1.07 (1.00)	0.17 (0.20)	0.95	0.97	1.55	1.83	189	241	262
$LaMnO_3$–PP-1	1.01 (1.00)	0.18 (0.20)	1.13	1.36	1.52	2.32	181	232	253
$LaMnO_3$–PP-2	0.92 (1.00)	0.18 (0.20)	1.39	1.31	1.72	1.87	169	222	243
$LaMnO_3$–PP-3	0.95 (1.00)	0.19 (0.20)	1.17	1.16	1.75	1.72	170	225	247
$LaMnO_3$–PP-2_850	0.93 (1.00)	0.19 (0.20)	1.13	1.03	1.50	1.85	190	241	258
$LaMnO_3$–PP-2_950	0.94 (1.00)	0.19 (0.20)	1.08	0.83	1.24	1.56	198	253	278

[a] These data in parenthesis are the nominal La/Mn or Mn/(La + Mn + O) atomic ratios.
[b] Data based on quantitative analysis of H_2-TPR profiles.

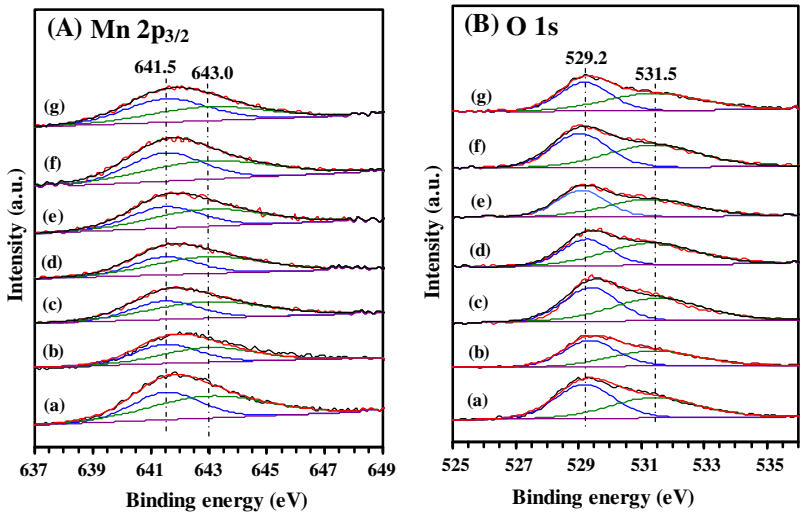

Fig. 5. (A) Mn $2p_{3/2}$ and (B) O 1s XPS spectra of (a) $LaMnO_3$–MeOH, (b) $LaMnO_3$–PEG, (c) $LaMnO_3$–PP-1, (d) $LaMnO_3$–PP-2, (e) $LaMnO_3$–PP-3, (f) $LaMnO_3$–PP-2_850, and (g) $LaMnO_3$–PP-2_950.

Mn/(La + Mn + O) molar ratios of the as-prepared samples were lower than 0.20.

Fig. 5 shows the Mn $2p_{3/2}$ and O 1s XPS spectra of the $LaMnO_3$ samples. It is commonly reported that there are Mn^{4+} and Mn^{3+} species in $LaMnO_3$. It is observed from Fig. 5A that there was an asymmetrical Mn $2p_{3/2}$ signal at BE = ca. 642 eV for each sample and this signal could be deconvoluted into two components at BE = 641.5 and 643.0 eV, the former was assignable to the Mn^{3+} species whereas the latter to the Mn^{4+} species [31]. By quantitatively analyzing the spectra, one can realize that there was a difference in surface Mn^{4+}/Mn^{3+} molar ratio of these $LaMnO_3$ samples, indicating that the preparation approach had an influence on surface Mn^{4+} concentration. With the addition of surfactant P123, the surface Mn^{4+}/Mn^{3+} molar ratios of the $LaMnO_3$–PP samples increased, with the $LaMnO_3$–PP-1 and $LaMnO_3$–PP-2 samples showing higher values (1.31–1.36). A rise in calcination temperature, however, resulted in a marked drop in surface Mn^{4+}/Mn^{3+} molar ratio. It means that the surface Mn^{4+} content tended to decrease with increasing calcination temperature, in agreement with the result observed by Wang et al. [32].

By using the curve-fitting approach, one can decompose the asymmetrical O 1s XPS peak at BE = ca. 530 eV of each sample into two components, one at 529.2 eV and the other at 531.5 eV (Fig. 5B). The peak at BE = 529.2 eV was attributed to the surface lattice oxygen (O_{latt}^{2-}) species, whereas that at BE = 531.5 eV to the adsorbed oxygen (O^-, O_2^- or O_2^{2-}) species [13,33]. These oxygen adspecies were strongly adsorbed on the surface oxygen vacancies of the perovskite-type oxide catalysts [33,34], and most of them could be retained on the catalyst surface at RT even under vacuum conditions. Among the $LaMnO_3$ samples investigated in the present study, the $LaMnO_3$–PP-2 sample exhibited the highest surface O_{ads}/O_{latt}^{2-} molar ratio (1.39), indicating that a higher surface area was beneficial for the enhancement of oxygen species on the surface, in consistence with the result observed in our previous study [26]. With the rise in calcination temperature, there was decline in the amount of surface oxygen adspecies; nonetheless, the amount was still higher than that of the bulk $LaMnO_3$ sample.

3.4. Reducibility

H_2-TPR experiments were conducted to investigate the reducibility of the $LaMnO_3$ samples, and the recorded profiles are illustrated in Fig. 6A. For each sample, two reduction steps were clearly observed, one in the range of 190–500 °C and the other in the range of 600–890 °C. For the $LaMnO_3$–MeOH, $LaMnO_3$–PEG, $LaMnO_3$–PP-1–3, and $LaMnO_3$–PP-2_850 samples, there was a shoulder centered in the 390–404 °C range. The reduction bands below 450 °C were due to the reduction of Mn^{4+} to Mn^{3+} as well as the removal of a small amount of oxygen adspecies, whereas the ones above 600 °C were due to the reduction of Mn^{3+} to Mn^{2+} [33,35]. The reduction bands of the bulk $LaMnO_3$ sample appeared at temperatures higher than those of the porous counterparts.

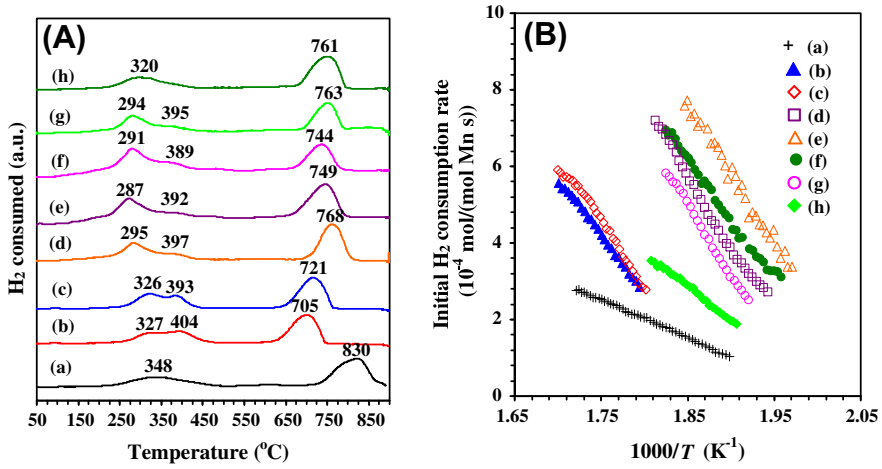

Fig. 6. (A) H_2-TPR profiles and (B) initial H_2 consumption rate as a function of inverse temperature of (a) $LaMnO_3$–bulk, (b) $LaMnO_3$–MeOH, (c) $LaMnO_3$–PEG, (d) $LaMnO_3$–PP-1, (e) $LaMnO_3$–PP-2, (f) $LaMnO_3$–PP-3, (g) $LaMnO_3$–PP-2_850, and (h) $LaMnO_3$–PP-2_950.

The difference in reduction temperature of these porous $LaMnO_3$ samples could be dependent on the preparation method. The H_2-TPR results demonstrate that the porous $LaMnO_3$ samples were more reducible than the bulk counterpart. Through quantitative analysis of the H_2-TPR profiles, one can obtain the H_2 consumption of each sample, as summarized in Table 2. When the manganese ions in $LaMnO_3$ were Mn^{3+} or Mn^{4+}, and completely reduced to Mn^{2+}, the theoretical H_2 consumption of $LaMnO_3$ would be 2.07 and 4.13 mmol/g, respectively. Clearly, the total H_2 consumption (2.8–3.84 mmol/g) calculated from the H_2-TPR profiles of the as-prepared $LaMnO_3$ catalysts fell into the theoretical H_2 consumption range of 2.07–4.13 mmol/g. Therefore, we deduce that there was the co-presence of Mn^{3+} and Mn^{4+} in the $LaMnO_3$ catalysts, coinciding with the results of XPS investigation (Fig. 5 and Table 2). For the bulk $LaMnO_3$ and porous $LaMnO_3$ samples, the H_2 consumption at lower temperatures (<500 °C) was 0.97 and 1.24–1.75 mmol/g, whereas that at higher temperatures ($\geqslant$500 °C) was 2.17 and 1.56–2.32 mmol/g, respectively. Apparently, the low-temperature H_2 consumption of the porous samples was much larger than that of the bulk sample. Furthermore, the porous samples with higher surface areas consumed more amounts of H_2 during the reduction process at low temperatures.

It is known that the reducibility of a catalyst can be effectively evaluated by using the initial (where less than 25% oxygen in the sample was consumed for the first reduction band) H_2 consumption rate [36]. Fig. 6B shows the initial H_2 consumption rate versus inverse temperature of the as-prepared $LaMnO_3$ samples. It can be clearly seen that the initial H_2 consumption rates of the samples followed the sequences of $LaMnO_3$–PP-2 > $LaMnO_3$–PP-2_850 > $LaMnO_3$–PP-2_950 as well as $LaMnO_3$–PP-2 > $LaMnO_3$–PP-3 > $LaMnO_3$–PP-1 > $LaMnO_3$–PEG $\approx$ $LaMnO_3$–MeOH > $LaMnO_3$–bulk. The trends are in good agreement with the orders of catalytic performance shown in Section 3.5.

3.5. Catalytic performance

In the blank experiment (only quartz sands were loaded), no conversion of toluene was observed below 400 °C, indicating that under the adopted reaction conditions, there is no occurrence of homogeneous reactions. Fig. 7 shows the catalytic performance of the as-synthesized $LaMnO_3$ samples for the oxidation of toluene. It can be clearly observed that toluene conversion increased with the rise in reaction temperature, and the porous $LaMnO_3$ catalysts performed much better than the bulk $LaMnO_3$ catalyst. According to the Weisz–Prater criterion, when the effectiveness factor $\eta \geqslant 0.95$ and reaction order $n = 1$, the dimensionless Weisz–Prater parameter (φ_{WP}) value is less than 0.3, which can be considered a sufficient condition for the absence of significant pore diffusion limitations [37]. At toluene conversion $\leqslant$20%, we carried out the Weisz–Prater analysis and calculated the φ_{WP} values, which were in the range of 0.011–0.056. Obviously, the φ_{WP} values obtained in our present work were much less than 0.3. Therefore, no significant mass transfer limitations existed in our catalytic system. It is worth pointing out that toluene was completely oxidized to CO_2 and H_2O over the as-prepared $LaMnO_3$ catalysts, and there is no detection of products of incomplete oxidation, as confirmed by the good carbon balance of ca. 99.5% in each run. It is convenient to compare the catalytic activities of these samples by adopting the reaction temperatures $T_{10\%}$, $T_{50\%}$, and $T_{90\%}$ (corresponding to the toluene conversion = 10%, 50%, and 90%), as summarized in Table 2. Among the $LaMnO_3$ samples, 3DOM-structured $LaMnO_3$–PP-2 with the highest BET surface area showed the best catalytic activity, and the $T_{50\%}$ and $T_{90\%}$ were ca. 222 and 243 °C, respectively, which were 45 and 55 °C lower than those achieved over the bulk $LaMnO_3$ catalyst derived by the conventional citric acid-complexing method (surface area = 7.3 m^2/g). Furthermore, the rise in calcination temperature resulted in drop of catalytic performance of $LaMnO_3$ (Fig. 7B and Table 2). When the calcination temperature rose from 750 to 850 or 950 °C, the $T_{50\%}$ and $T_{90\%}$ values increased to 241 and 258 °C, and 253 and 278 °C, respectively. The rise in calcination temperature caused the undermining of the 3DOM structure and the growth of $LaMnO_3$ crystallites (Figs. 2k–n, 3p, q, s, and t), as reflected in the significant decrease in BET surface area from 39.4 m^2/g (at 750 °C) to 27.3 m^2/g (at 850 °C) or to 19.0 m^2/g (at 950 °C). The changing trends in toluene consumption rate versus reaction temperature (Fig. 7C and D) were similar to those in toluene conversion versus reaction temperature (Fig. 7A and B) obtained over these $LaMnO_3$ catalysts. It is hence concluded that the catalytic activity decreased in the orders of $LaMnO_3$–PP-2 > $LaMnO_3$–PP-2_850 > $LaMnO_3$–PP-2_950 as well as $LaMnO_3$–PP-2 > $LaMnO_3$–PP-3 > $LaMnO_3$–PP-1 > $LaMnO_3$–PEG > $LaMnO_3$–MeOH > $LaMnO_3$–bulk (Fig. 7A and B and Table 2), coinciding with the sequences of low-temperature reducibility (i.e., initial H_2 consumption rate). According to the activity data and moles of Mn in the $LaMnO_3$ catalysts, we calculated the turnover frequencies (TOFs), and the results are shown in Table 3 and Fig. S5 of the Supplementary data. It is observed that the TOF value over each of the as-prepared catalysts increased with a rise in reaction temperature. Under the same temperature, the TOF values over the 3DOM-structured

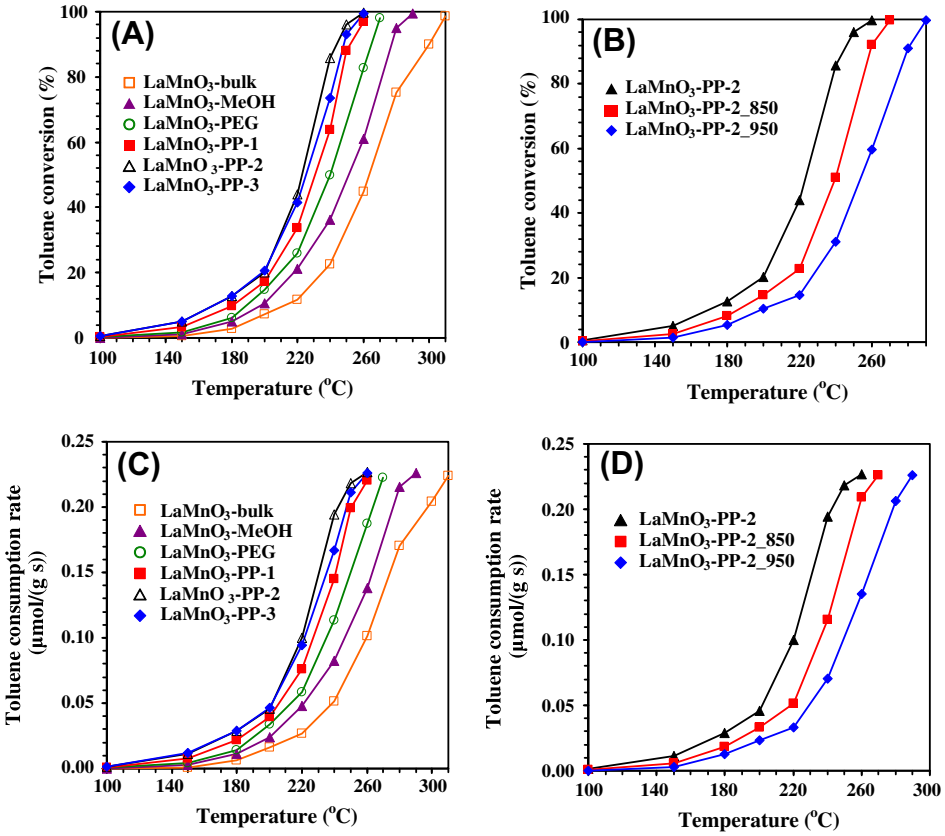

Fig. 7. (A and B) Toluene conversion and (C and D) toluene consumption rate as a function of reaction temperature over the as-prepared $LaMnO_3$ catalysts under the conditions of toluene concentration = 1000 ppm, toluene/oxygen molar ratio = 1:400, and SV = 20,000 mL/(g h).

Table 3
Turnover frequencies (TOFs), rate constants (k), pre-exponential factors (A), and activation energies (E_a) for the oxidation of toluene over the as-prepared $LaMnO_3$ samples in the temperature range of 100–200 °C.

Catalyst	TOF ($\mu mol_{toluene}/(mol_{Mn}\ s)$)				k (s^{-1})				A (s^{-1})	E_a (kJ/mol)
	100 °C	150 °C	180 °C	200 °C	100 °C	150 °C	180 °C	200 °C		
$LaMnO_3$–bulk	0.0058	0.24	1.52	3.93	1.07×10^{-4}	4.43×10^{-3}	2.85×10^{-2}	7.72×10^{-2}	4.25×10^{9}	97
$LaMnO_3$–MeOH	0.047	0.68	2.80	5.81	8.61×10^{-4}	1.26×10^{-2}	5.38×10^{-2}	1.18×10^{-1}	1.17×10^{7}	72
$LaMnO_3$–PEG	0.10	0.98	3.38	8.15	1.90×10^{-3}	1.82×10^{-2}	6.56×10^{-2}	1.74×10^{-1}	2.32×10^{6}	65
$LaMnO_3$–PP-1	0.17	1.87	5.31	9.51	3.11×10^{-3}	3.52×10^{-2}	1.07×10^{-1}	2.09×10^{-1}	1.44×10^{6}	62
$LaMnO_3$–PP-2	0.28	2.75	7.00	11.03	5.13×10^{-3}	5.27×10^{-2}	1.46×10^{-1}	2.52×10^{-1}	6.13×10^{5}	58
$LaMnO_3$–PP-3	0.29	2.82	7.00	11.27	5.23×10^{-3}	5.42×10^{-2}	1.46×10^{-1}	2.58×10^{-1}	6.15×10^{5}	57
$LaMnO_3$–PP-2_850	0.13	1.33	4.51	7.95	2.33×10^{-3}	2.49×10^{-2}	8.94×10^{-2}	1.69×10^{-1}	1.69×10^{6}	63
$LaMnO_3$–PP-2_950	0.040	0.71	3.00	5.66	7.26×10^{-4}	1.31×10^{-2}	5.77×10^{-2}	1.15×10^{-1}	2.44×10^{7}	75

$LaMnO_3$ catalysts were much higher than that over the bulk counterpart, with the $LaMnO_3$–PP-2 and $LaMnO_3$–PP-3 catalysts giving the highest TOF values.

The effects of SV and toluene/O_2 molar ratio on the catalytic activity of the $LaMnO_3$–PP-2 sample were examined, and the results are shown in Fig. 8. As expected, there was a general trend of activity decrease at elevated SV values (Fig. 8A). At SV = 5000 h^{-1}, the $T_{50\%}$ and $T_{90\%}$ values were 209 and 233 °C, respectively, which were ca. 13 and 10 °C lower than those achieved at SV = 20,000 h^{-1}. Further rise of SV to 40,000 h^{-1} resulted in a drop in catalytic activity of the $LaMnO_3$–PP-2 sample. As for the influence of oxygen concentration, a drop of toluene/O_2 molar ratio from 1:50 to 1:100 caused the $T_{90\%}$ value to decrease from 274 to 256 °C; when the toluene/O_2 molar ratio was 1:400, the $T_{90\%}$ value decreased to 243 °C (Fig. 8B). It is clear that the increase in O_2 concentration of the reactant feed had a positive effect on the enhancement of toluene conversion. The result implies that the oxygen adspecies on the catalyst surface played an important role in the total oxidation of toluene. In other words, the oxygen nonstoichiometry related to structural defects might be a critical factor in determining the catalytic performance of the $LaMnO_3$ sample. A higher oxygen concentration in feedstock might be beneficial for the better replenishing of active oxygen adspecies that were consumed due to their reaction with toluene. To examine the stability of catalytic performance, we carried out the experiments with temperature going down and then up again, and the results are shown in Fig. S6 of the Supplementary data. Obviously, the catalytic activities measured with temperature going down and then up again of the samples were rather close, indicating that the catalysts were stable. The on-stream reaction experiment conducted over the $LaMnO_3$–PP-2 catalyst indicates that there was no significant drop in catalytic activity within 48 h (Fig. 9). In addition, the XRD pattern (Fig. S7 of Supplementary data) of the used $LaMnO_3$–PP-2 sample was similar to that of the as-prepared

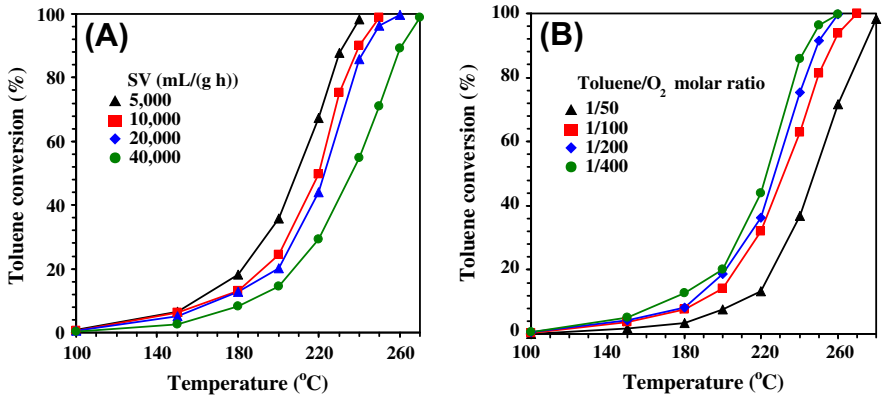

Fig. 8. Catalytic performance of the $LaMnO_3$–PP-2 sample as a function of reaction temperature at (A) toluene concentration = 1000 ppm, toluene/O_2 molar ratio = 1:400, and different SV values and (B) toluene concentration = 1000 ppm, SV = 20,000 mL/(g h), and various toluene/O_2 molar ratios.

counterpart. Therefore, we conclude that the as-prepared 3DOM-structured $LaMnO_3$ samples were catalytically durable.

The catalytic performance ($T_{50\%}$ = 222 °C and $T_{90\%}$ = 243 °C at SV = 20,000 mL/(g h); $T_{50\%}$ = 236 °C and $T_{90\%}$ = 261 °C at SV = 40,000 mL/(g h)) over our 3DOM-structured $LaMnO_3$–PP-2 catalyst was much better than those ($T_{50\%}$ = 254 °C and $T_{90\%}$ = 295 °C at 178 h^{-1}) over $LaMnO_3$ [6], ($T_{50\%}$ = 279 °C and $T_{90\%}$ = 306 °C at 178 h^{-1}) over $LaCoO_3$ [6], ($T_{50\%}$ = 233 °C and $T_{90\%}$ = 258 °C at 36,000 mL/(g h)) over 30 wt.% Co_3O_4–CeO_2 [38], ($T_{50\%}$ = 270 °C and $T_{90\%}$ = 300 °C at 186 h^{-1}) over 5 wt.% Au/CeO_2 [39], similar to that ($T_{50\%}$ = 175 °C and $T_{90\%}$ = 250 °C at 18,000 mL/(g h)) over 0.5 wt.% Pd/$LaMnO_3$ [40], but inferior to those ($T_{50\%}$ = 235 °C and $T_{90\%}$ = 250 °C at 50,000 mL/(g h)) over 50 wt.% MnO_x–50 wt.% CeO_2 [41] and ($T_{50\%}$ = 202 °C and $T_{90\%}$ = 221 °C at 20,000 mL/(g h)) over the Sr-doped lanthanum manganate ($La_{0.8}Sr_{0.2}MnO_3$) [3].

It is well known that the catalytic performance of an ABO_3 material is associated with the surface area, defect nature and density, oxygen adspecies, and reducibility. A higher surface area is beneficial for the improvement of catalytic activity [11,42]. The presence of oxygen deficiencies favors the activation of gas-phase oxygen molecules for the generation of active oxygen adspecies, the higher the oxygen vacancy density, the better the catalytic performance of a perovskite sample [8,43]. The strong redox ability of ABO_3 guarantees the recyclability of B-site ions (with at least two oxidation states), thus facilitating the oxidation of organic compounds [44]. Compared to bulk $LaMnO_3$, the 3DOM-structured $LaMnO_3$–PP-1–3 samples are much smaller in particle size, higher in surface area, larger in surface oxygen adspecies and Mn^{4+} concentration as well as much better in terms of low-temperature reducibility (Tables 1 and 2 and Figs. 1–6). These unique characters of the 3DOM-structured $LaMnO_3$–PP-1–3 samples render them better activity in catalyzing the total oxidation of toluene. We deduce that the excellent catalytic performance of the $LaMnO_3$–PP-1–3 samples is a combined result of the high-quality 3DOM architecture with nanovoid skeletons, high oxygen adspecies concentration, and good low-temperature reducibility.

3.6. Kinetic parameters

In the past years, there have been reports on the kinetics of catalytic oxidation of VOCs. For example, Wong et al. claimed that the oxidation of butyl acetate over the AgZSM-5 catalyst was first order toward butyl acetate concentration and zero toward oxygen concentration [45]; by assuming a first-order kinetics with respect to toluene and a zero-order kinetics with respect to oxygen, Alifanti et al. obtained good linear Arrhenius plots for the oxidation of toluene over ceria–zirconia-supported $LaCoO_3$ catalysts [46].

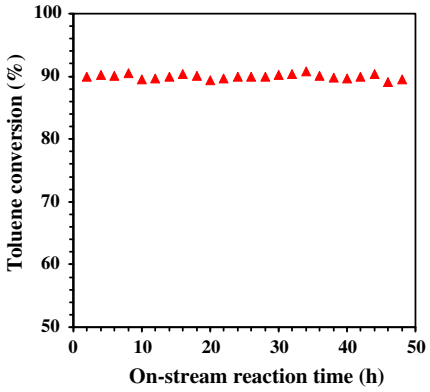

Fig. 9. Catalytic activity as a function of on-stream reaction time over the $LaMnO_3$–PP-2 catalyst for toluene oxidation under the conditions of toluene concentration = 1000 ppm, toluene/O_2 molar ratio = 1:400, reaction temperature = 243 °C, and SV = 20,000 mL/(g h).

Therefore, it is reasonable to suppose that the oxidation of toluene in the presence of excess oxygen (toluene/O_2 molar ratio = 1:50–1:400) would obey a first-order reaction mechanism with respect to toluene concentration (c):

$$r = -kc = (-A\exp(-E_a/RT))c \quad (1)$$

where r is the reaction rate (mol/s), k the rate constant (s^{-1}), A the pre-exponential factor, and E_a the apparent activation energy (kJ/mol). The k values could be calculated from the reaction rates and reactant conversions at different SV and reaction temperatures.

Fig. 10 shows the Arrhenius plots for the oxidation of toluene at toluene conversion <20% (at which the reaction temperature range was 100–200 °C) over the as-prepared $LaMnO_3$ catalysts. According to the slopes of the Arrhenius plots, one can calculate the rate constants, pre-exponential factors, and apparent activation energies of toluene oxidation over these catalysts, as summarized in Table 3. It can be clearly seen that the k value increased with the rise in temperature for each catalyst; at the same temperature, however, the k values for the porous $LaMnO_3$ catalysts were much higher than that for the bulk $LaMnO_3$ catalyst (despite its A value was the highest), with the highest k values being achieved over the 3DOM-structured $LaMnO_3$–PP-2 and $LaMnO_3$–PP-3 catalysts (despite lower A values). The E_a value (97 kJ/mol) of the bulk $LaMnO_3$ catalyst was much higher than those (57–75 kJ/mol) of the porous $LaMnO_3$ catalysts, with the 3DOM-structured $LaMnO_3$–PP-1 and $LaMnO_3$–PP-3 catalysts exhibiting the lowest E_a values (57–58 kJ/mol). The E_a values obtained over the 3DOM-structured $LaMnO_3$–PP-1–3 catalysts for toluene oxidation were much lower than those

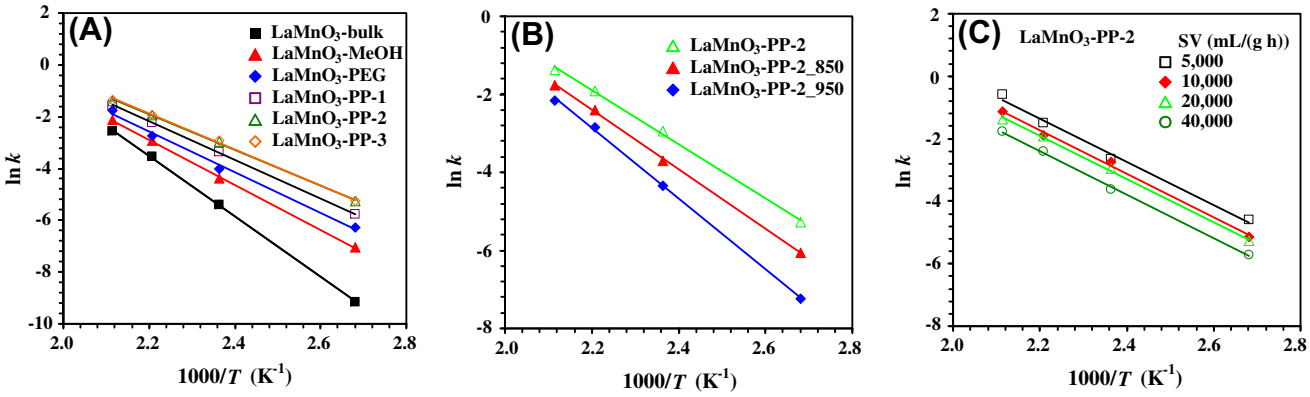

Fig. 10. Arrhenius plots for total oxidation of toluene on the as-prepared $LaMnO_3$ catalysts.

(120–144 kJ/mol) over the Al_2O_3-supported CuO or MnO catalysts [47] and (73–89 kJ/mol) over the $M_xFe_{3-x}O_4$ (M = Ni, Mn; x = 0.5–0.65) catalysts [48], but similar to those (51–79 kJ/mol) over the 10–20 wt.% $LaCoO_3/Ce_{1-x}Zr_xO_2$ (x = 0–0.2) catalysts [46] and that (62 kJ/mol) over the 7 wt.% Pt/16 wt.% $Ce_{0.64}Zr_{0.15}Bi_{0.21}O_{1.895}/\gamma$-$Al_2O_3$ catalyst [49]. All the results explain why the 3DOM-structured $LaMnO_3$ catalysts performed excellently in catalyzing the complete oxidation of toluene at low temperatures.

4. Conclusions

Rhombohedrally crystallized 3D macroporous $LaMnO_3$ materials were prepared by adopting the surfactant-assisted PMMA-templating methods. The nature of surfactant has an influence on the porous structure of the $LaMnO_3$ samples. In the absence of P123 but the presence of PEG400, there is the generation of 3DOM-structured $LaMnO_3$–PEG without nanovoids on the macropore walls; with the use of PEG400 and P123, however, the as-obtained $LaMnO_3$–PP-1–3 are with high-quality 3DOM structures, nanovoid skeletons, and high surface areas (37–39 m^2/g). There is the co-presence of Mn^{4+} and Mn^{3+} species on the $LaMnO_3$ surfaces, and the surface Mn^{4+}/Mn^{3+} molar ratios of $LaMnO_3$–PP-1 and $LaMnO_3$–PP-2 are much higher than those of the other $LaMnO_3$ samples. It was also found that the oxygen adspecies concentration on the $LaMnO_3$–PP-2 surface was the highest. The porous $LaMnO_3$ samples exhibited better low-temperature reducibility than the bulk $LaMnO_3$ counterpart, with the best low-temperature reducibility being achieved over the nanovoid-containing 3DOM-structured $LaMnO_3$–PP-2 sample. Under the conditions of toluene concentration = 1000 ppm, toluene/O_2 molar ratio = 1:400, and SV = 20,000 mL/(g h), the porous $LaMnO_3$ catalysts outperformed the bulk $LaMnO_3$ counterpart, and the 3DOM-structured $LaMnO_3$–PP-1–3 with nanovoid skeletons showed the best catalytic activity ($T_{50\%}$ = 222–232 °C and $T_{90\%}$ = 243–253 °C). The apparent activation energies (57–62 kJ/mol) obtained over the 3DOM-structured $LaMnO_3$–PP-1–3 catalysts were much lower than that (97 kJ/mol) obtained over the bulk $LaMnO_3$ catalyst for toluene combustion. The excellent catalytic performance of the $LaMnO_3$–PP-1–3 samples can be attributed to the presence of high-quality 3DOM architecture, nanovoid skeleton, high oxygen adspecies concentration, and good low-temperature reducibility.

Acknowledgments

The work described was supported by the NSF of China (20973017 and 21077007), the Creative Research Foundation of Beijing University of Technology (00500054R4003 and 005000543111501), "863" Key Program of Ministry of Science and Technology of China (2009AA063201), and the Funding Project for Academic Human Resources Development in Institutions of Higher Learning under the Jurisdiction of Beijing Municipality (PHR201007105 and PHR201107104). CTAU thanks the Hong Kong Baptist University for financial support (FRG2/09-10/023). We also thank Mrs. Jianping He (State Key Laboratory of Advanced Metals and Materials, University of Science & Technology Beijing) for doing the SEM analysis.

Appendix A. Supplementary material

Supplementary data associated with this article can be found, in the online version, at doi:10.1016/j.jcat.2011.12.015.

References

[1] J.-M. Giraudon, A. Elhachimi, G. Leclercq, Appl. Catal. B 84 (2008) 251–261.
[2] A.K. Sinha, K. Suzuki, Appl. Catal. B 70 (2007) 417–422.
[3] V. Blasin-Aubé, J. Belkouch, L. Monceaux, Appl. Catal. B 43 (2003) 175–186.
[4] H. Najjar, H. Batis, Appl. Catal. A 383 (2010) 192–201.
[5] R. Spinicci, M. Faticanti, P. Marini, S. De Rossi, P. Porta, J. Mol. Catal. A 197 (2003) 147–155.
[6] S. Irusta, M.P. Pina, M. Menéndez, J. Santamaría, J. Catal. 179 (1998) 400–412.
[7] J.G. Deng, L. Zhang, H.X. Dai, H. Hong, C.T. Au, Ind. Eng. Chem. Res. 47 (2008) 8175–8183.
[8] M.A. Peña, J.L.G. Fierro, Chem. Rev. 101 (2001) 1981–2018.
[9] Y.G. Wang, J.W. Ren, Y.Q. Wang, F.Y. Zhang, X.H. Liu, Y. Gao, G.Z. Lu, J. Phys. Chem. C 112 (2008) 15293–15298.
[10] G.J. Zou, L. Chen, X.L. Wang, Catal. Lett. 127 (2009) 444–447.
[11] N. Gunasekaran, S. Saddawi, J.J. Carberry, J. Catal. 159 (1996) 107–111.
[12] P. Ciambelli, S. Cimino, S.-D. Rossi, M. Faticanti, L. Lisi, G. Minelli, I. Pettiti, P. Porta, G. Russo, M. Turco, Appl. Catal. B 24 (2000) 243–253.
[13] A. Machocki, T. Ioannides, B. Stasinska, W. Gac, G. Avgouropoulos, D. Delimaris, W. Grzegorczyk, S. Pasieczna, J. Catal. 227 (2004) 282–296.
[14] J.N. Kuhn, U.S. Ozkan, J. Catal. 253 (2008) 200–211.
[15] R.Z. Hou, P. Ferreira, P.M. Vilarinho, Chem. Mater. 21 (2009) 3536–3541.
[16] X.X. Fan, Y. Wang, X.Y. Chen, L. Gao, W.J. Luo, Y.P. Yuan, Z.S. Li, T. Yu, J.H. Zhu, Z.G. Zou, Chem. Mater. 22 (2010) 1276–1278.
[17] M. Sadakane, T. Asanuma, J. Kubo, W. Ueda, Chem. Mater. 17 (2005) 3546–3551.
[18] Y.N. Kim, S.J. Kim, E.K. Lee, E.O. Chi, N.H. Hur, C.S. Hong, J. Mater. Chem. 14 (2004) 1774–1777.
[19] Y.C. Wei, J. Liu, Z. Zhao, Y.S. Chen, C.M. Xu, A.J. Duan, G.Y. Jiang, H. He, Angew. Chem. Int. Ed. 50 (2011) 16.
[20] J.F. Xu, J. Liu, Z. Zhao, J.X. Zheng, G.Z. Zhang, A.J. Duan, G.Y. Jiang, Catal. Today 153 (2010) 136–142.
[21] O. Sel, D. Kuang, M. Thommers, B. Smarsly, Langmuir 22 (2006) 2311–2322.
[22] Z.Y. Wang, A. Stein, Chem. Mater. 20 (2008) 1029–1040.
[23] G.Z. Wang, L. Zhang, H.X. Dai, J.G. Deng, C.X. Liu, H. He, C.T. Au, Inorg. Chem. 47 (2008) 4015–4022.
[24] C.X. Liu, L. Zhang, J.G. Deng, Q. Mu, H.X. Dai, H. He, J. Phys. Chem. C 112 (2008) 19248–19256.
[25] H.N. Li, L. Zhang, H.X. Dai, H. He, Inorg. Chem. 48 (2009) 4421–4434.
[26] R.Z. Zhang, H.X. Dai, Y.C. Du, L. Zhang, J.G. Deng, Y.S. Xia, Z.X. Zhao, X. Meng, Y.X. Liu, Inorg. Chem. 50 (2011) 2534–2544.
[27] M. Sadakane, T. Horiuchi, N. Kato, K. Sasaki, W. Ueda, J. Solid State Chem. 183 (2010) 1365–1371.

[28] M. Sadakane, C. Takahashi, N. Kato, H. Ogihara, Y. Nodasaka, Y. Doi, Y. Hinatsu, W. Ueda, Bull. Chem. Soc. Jpn. 80 (2007) 677–685.
[29] M.C. Orilall, N.M. Abrams, J. Lee, F.J. Disalvo, U. Wiesner, J. Am. Chem. Soc. 130 (2008) 8882–8883.
[30] M. Sadakane, T. Horiuchi, N. Kato, C. Takahashi, W. Ueda, Chem. Mater. 19 (2007) 5779–5785.
[31] H.B. Deng, L. Lin, Y. Sun, C.S. Pang, J.P. Zhuang, P.K. Ouyang, Z.J. Li, S.J. Liu, Catal. Lett. 126 (2008) 106–111.
[32] X.L. Wang, D. Li, C.X. Shi, B. Li, T.Y. Cui, Z.D. Zhang, Physica B 405 (2010) 1362–1368.
[33] Y.J. Zhu, Y.Q. Sun, X.Y. Niu, F.L. Yuan, H.G. Fu, Catal. Lett. 135 (2010) 152–158.
[34] B.P. Barbero, J.A. Gamboa, L.E. Cadús, Appl. Catal. B 65 (2006) 21–30.
[35] A. Kaddouri, S. Ifrah, P. Gelin, Catal. Lett. 119 (2007) 237–244.
[36] H.X. Dai, A.T. Bell, E. Iglesia, J. Catal. 221 (2004) 491–499.
[37] S. Mukherjee, M.Albert Vannice, J. Catal. 243 (2006) 108–130.
[38] L.F. Liotta, M. Ousmane, G. Di Carlo, G. Pantaleo, G. Deganello, A. Boreave, A. Giroir-Fendler, Catal. Lett. 127 (2009) 270–276.
[39] S. Scirè, S. Minicò, C. Crisafulli, C. Satriano, A. Pistone, Appl. Catal. B 40 (2003) 43–49.
[40] A. Musialik-Piotrowska, H. Landmesser, Catal. Today 137 (2008) 357–361.
[41] D. Delimaris, T. Ioannides, Appl. Catal. B. 84 (2008) 303–312.
[42] N. Yi, Y. Cao, Y. Su, W.-L. Dai, H.-Y. He, K.-N. Fan, J. Catal. 230 (2005) 249–253.
[43] J.G. Deng, L. Zhang, H.X. Dai, H. He, C.T. Au, Appl. Catal. B 89 (2009) 87–96.
[44] T. Nakamura, M. Misono, Y. Yoneda, Chem. Lett. 10 (1981) 1589–1592.
[45] C.T. Wong, A.Z. Abdullah, S. Bhatia, J. Hazard. Mater. 157 (2008) 480–489.
[46] M. Alifanti, M. Florea, S. Somacescu, V.I. Pârvulescu, Appl. Catal. B 60 (2005) 33–39.
[47] S.M. Saqer, D.I. Kondarides, X.E. Verykios, Appl. Catal. B 103 (2011) 275–286.
[48] M. Florea, M. Alifanti, V.I. Pârvulescu, D. Mihaila-Tarabasanu, L. Diamandescu, M. Feder, C. Negrila, L. Frunza, Catal. Today 141 (2009) 361–366.
[49] T. Masui, H. Imadzu, N. Matsuyama, N. Imanaka, J. Hazard. Mater. 176 (2010) 1106–1109.